Transient volcano deformation sources imaged with interferometric synthetic aperture radar: Application to Seguam Island, Alaska

Timothy Masterlark and Zhong Lu

Science Applications International Corporation, U.S. Geological Survey EROS Data Center, Sioux Falls, South Dakota, USA

Received 2 May 2003; revised 11 August 2003; accepted 3 October 2003; published 2 January 2004.

[1] Thirty interferometric synthetic aperture radar (InSAR) images, spanning various intervals during 1992–2000, document coeruptive and posteruptive deformation of the 1992–1993 eruption on Seguam Island, Alaska. A procedure that combines standard damped least squares inverse methods and collective surfaces, identifies three dominant amorphous clusters of deformation point sources. Predictions generated from these three point source clusters account for both the spatial and temporal complexity of the deformation patterns of the InSAR data. Regularized time series of source strength attribute a distinctive transient behavior to each of the three source clusters. A model that combines magma influx, thermoelastic relaxation, poroelastic effects, and petrologic data accounts for the transient, interrelated behavior of the source clusters and the observed deformation. Basaltic magma pulses, which flow into a storage chamber residing in the lower crust, drive this deformational system. A portion of a magma pulse is injected into the upper crust and remains in storage during both coeruption and posteruption intervals. This injected magma degasses and the volatile products accumulate in a shallow poroelastic storage chamber. During the eruption, another portion of the magma pulse is transported directly to the surface via a conduit roughly centered beneath Pyre Peak on the west side of the island. A small amount of this magma remains in storage during the eruption, and posteruption thermoelastic contraction ensues. This model, made possible by the excellent spatial and temporal coverage of the InSAR data, reveals a relatively simple system of interrelated predictable processes driven by magma dynamics. *INDEX TERMS:* 1213 Geodesy and Gravity: Earth's interior—dynamics (8115, 8120); 3210 Mathematical Geophysics: Modeling; 8135 Tectonophysics: Hydrothermal systems (8424); *KEYWORDS:* volcano deformation, InSAR, static deformation

Citation: Masterlark, T., and Z. Lu (2004), Transient volcano deformation sources imaged with interferometric synthetic aperture radar: Application to Seguam Island, Alaska, *J. Geophys. Res.*, *109*, B01401, doi:10.1029/2003JB002568.

1. Introduction

[2] An interferometric synthetic aperture radar (InSAR) image can map deformation with a high level of spatial resolution (a few to tens of meters) and centimeter to subcentimeter precision during the time interval separating the acquisition of two synthetic aperture radar images [*Massonnet and Feigl*, 1998; *Lu et al.*, 2002a; *Rosen et al.*, 2000]. Multiple InSAR images spanning a variety of time intervals can be used to characterize transient deformation [*Feigl et al.*, 2000; *Lu et al.*, 2003b]. InSAR imagery is particularly valuable for monitoring the deformation of volcanoes having remote locations and, as a consequence, no other instrumentation. Interpretations of InSAR images are especially useful at volcanoes where crustal displacements indicate magmatic activity. The observed deformation alone is interesting, but more importantly, the observed deformation can be used to infer subsurface processes that cannot be directly observed. Mechanical modeling, constrained by the InSAR imagery, is a powerful tool that can quantify the spatial and temporal deformational mechanisms within a volcano.

[3] The standard approach to modeling volcano deformation, detected with InSAR, involves using a forward model to relate the observed deformation to a source at depth [*Dzurisin*, 2003, and references therein]. The forward model is then inverted to obtain the source strength, the interpretation of which can be biased by assumptions and implications associated with the presupposed model. For example, an InSAR image of a volcano with a radially symmetric deformation pattern is often attributed to magma intrusion, or alternatively, a change in pore fluid pressure in a spherical chamber or aquifer, respectively [*Lu et al.*, 2002, 2003b]. Sources having tabular or triaxial elliptical geometries are invoked to account for nonradial InSAR deformation patterns [*Fialko and Simons*, 2000; *Wicks et al.*, 2001]. Combinations of sources with various geometries have been proposed to model complex deformation patterns [*Feigl et al.*, 2000; *Lu et al.*, 2000b; *Mann and Freymueller*, 2003].

[4] The relatively complex surface displacement fields associated with changing pore fluid pressures in subsurface

0148-0227/04/2003JB002568$09.00

fracture systems, observed near geothermal areas, led to a recent departure from this relatively simple modeling approach. Rather than assigning sources with a priori geometries, *Vasco et al.* [2002] divided the region beneath the surface into a three-dimensional array of source cells. Using InSAR images and standard linear inverse methods, they identified dominant amorphous source distributions. *Mossop and Segall* [1999] used a similar approach to account for deformation suggested by leveling and GPS data for the Geysers geothermal field in northern California. Both of these studies use singular value decomposition and truncated data kernel spectra [*Menke*, 1989] to map the observed deformation data into a distribution of volumetric changes in subsurface three-dimensional arrays of source nodes. Both studies assume the volumetric changes are caused by changes in pore fluid pressure.

[5] Thirty InSAR images of Seguam Island, Alaska, reveal a seemingly complex evolution of deformation during the period 1992–2000. In an effort to account for the observed deformation, we extend the concept of a three-dimensional source array to identify discrete deformation "source clusters" at depth, each having a distinctive transient behavior. This method allows for multiple elastic deformation mechanisms (magma chamber pressurization, thermoelasticity, and poroelasticity) within and among the source clusters. We combine this method with the 30 InSAR images to estimate the evolution of deformation sources beneath Seguam Island during 1992–2000.

2. Seguam Island

[6] Seguam Island is located in the central Aleutian arc (Figure 1), which is segmented into a series of blocks that are rotating in a clockwise direction in response to oblique Pacific-North American plate convergence [*Geist et al.*, 1988; *Ryan and Scholl*, 1993; *Lu and Wyss*, 1996]. The 20 km × 30 km island occupies the saddle between the Amlia and Amukta basins, a region of extension just north of the trailing edge of the rotating Andreanof block [*Singer et al.*, 1992b; *Ryan and Scholl*, 1993]. The major axis of Seguam Island, as well as an alignment of seven volcanic vents, is subparallel to the Aleutian trench. This alignment is roughly perpendicular to the local minimum principal stress caused by the rotation of the Andreanof block.

[7] The morphology of the island is dominated by two calderas. All historical eruptions are thought to have emanated from or near Pyre Peak (elevation 1042 m) [*Miller et al.*, 1998], the volcanic cone located near the center of the western caldera. The eastern caldera occupies the majority of the eastern half of the island. *Singer et al.* [1992b] provide a comprehensive discussion of the geologic evolution of Seguam Island. A brief summary of the four-phase evolution is given here. The first (oldest) phase is submarine volcanism from about 5.0 to 1.1 Ma. The second eruptive phase includes lava and pyroclastic flows of the Turf Point Formation having ages of 1.07–0.07 Ma. A third eruptive phase includes lava and pyroclastic flows of the Finch Cove Formation from 0.08 to 0.03 Ma. A stratovolcano near the eastern margin of the eastern caldera grew during this phase and collapsed at the end of the phase. The fourth phase includes the Holocene age Pyre Peak Formation.

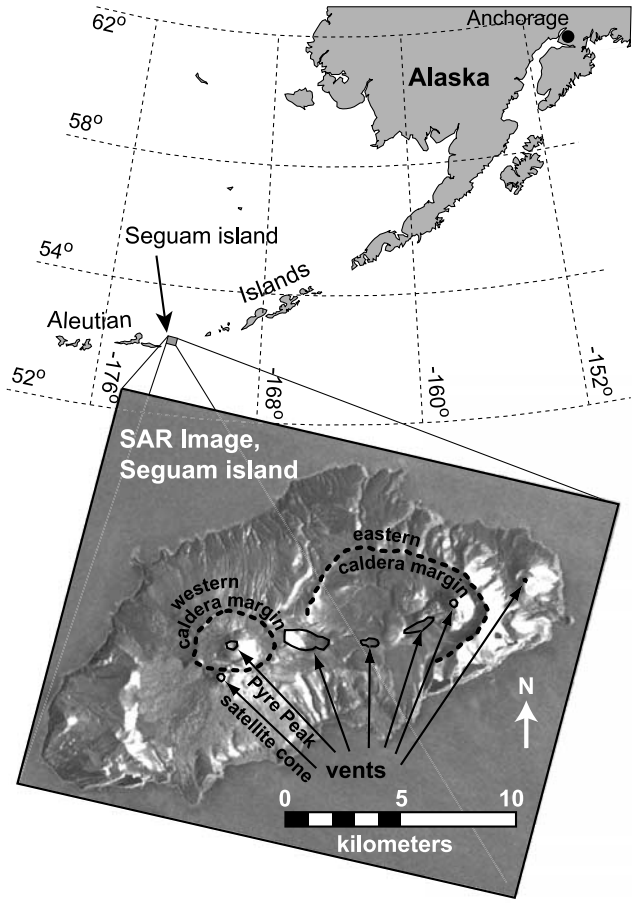

Figure 1. Study site. Seguam Island is located near the midway point of the Aleutian island arc, Alaska. The island consists of two calderas. Historical eruptions are thought to have emanated from or near Pyre Peak, a volcanic cone located near the center of the western caldera. The historically inactive eastern caldera dominates the eastern half of the island. The string of volcanic vents is roughly perpendicular to the local minimum principal stress.

[8] Documented eruptions occurred in 1786–1790, 1827, 1891, 1892, 1901, 1927, 1977, and 1992–1993. The March 1977 eruption was marked by effusive lava fountains and flows from the satellite cone located about 1.5 km southwest of Pyre Peak (Figure 1) [*Miller et al.*, 1998]. The most recent eruption spanned an interval from December 1992 through August 1993. The activity was intermittent and began with an ash eruption from the statellite cone on 27 December 1992. The ash plume rose to an altitude of 1200 m. Another small ash eruption followed a few days later on 30 December 1992. The plume from this eruption rose to an altitude of a few hundred meters. On 28 May 1993, a small ash eruption was observed. On 2 June 1993, a plume rising to a height of 3000 m was observed. The next reported episode of activity began with heavy ash eruptions, attaining an altitude of about 1000 m, on 31 July 1993. This eruption episode also produced a lava flow and continued sporatically through 10 August 1993, on which an ash plume rose to 2400 m. It is likely that additional events may have gone unnoticed due to the remote location and inclement weather of the region (Smithsonian Institution,

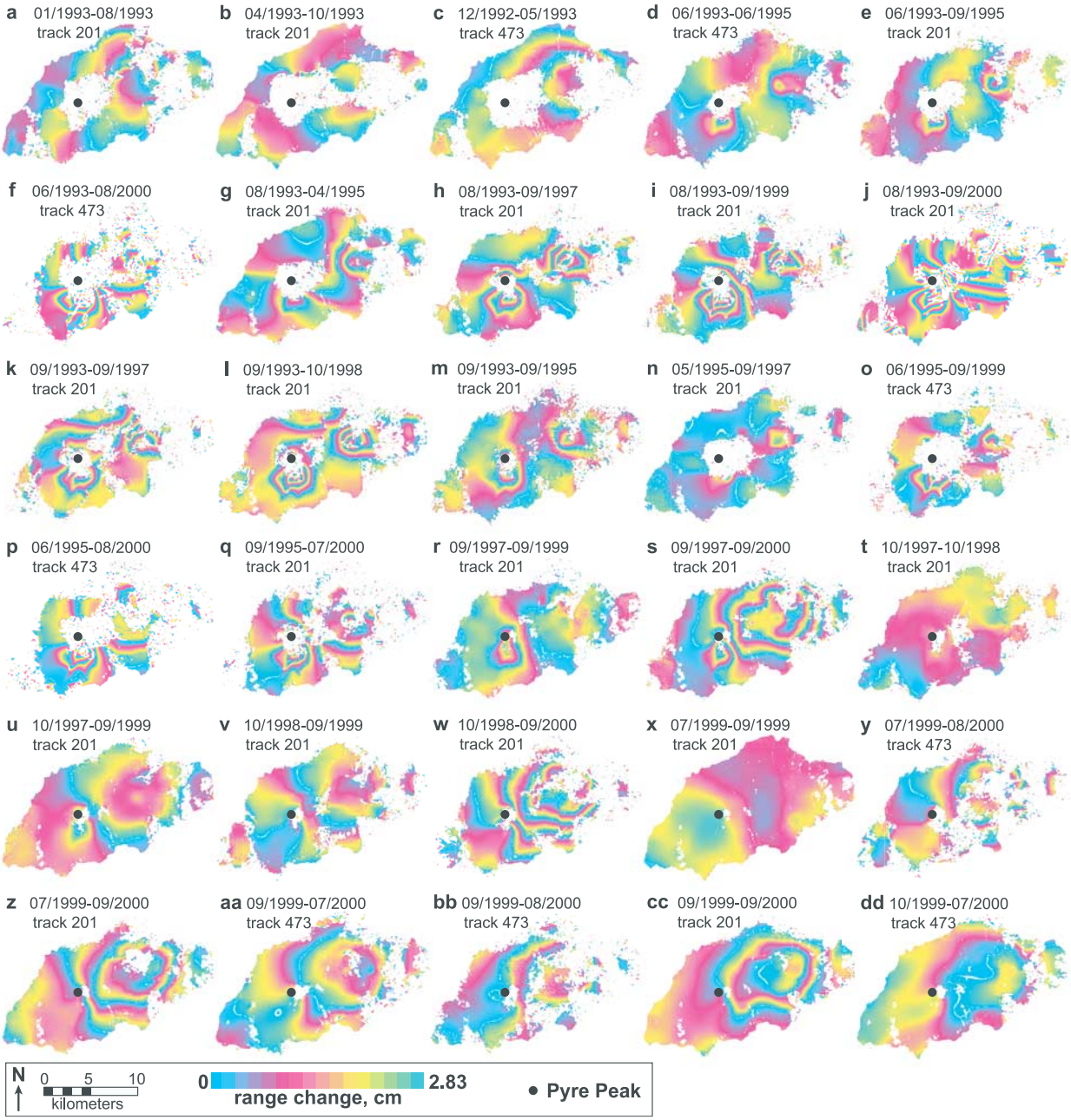

Figure 2. InSAR images. Thirty InSAR images from tracks 201 and 473 span a variety of epochs during 1992–2000. The explanation at the bottom applies to all InSAR images. Each fringe, blue-red-yellow-blue, represents 2.83 cm of range change away from a fixed satellite position. (a–c) Coeruption images. These images suggest broad deformation roughly centered beneath the eastern caldera, which has not erupted in historical time. (d-dd) Posteruption images. Deformation during the first few years following the eruption includes a complicated pattern of transient deformation regions. Images spanning the later portions of the posteruption period are similar to the coeruption deformation.

http://www.volcano.si.edu/gvp/world/region11/aleutian/seguam/var.htm#index).

3. Data

3.1. InSAR Images

[9] We obtained 40 ERS-1 and ERS-2 SAR images that span the period 1992–2000. We processed the SAR data together with a 1 arc sec (about 30 m) SRTM digital elevation model (DEM) using the two-pass InSAR method described by *Massonnet and Feigl* [1998]. The SRTM DEM has a relative vertical height accuracy of better than 10 m [*Farr and Kobrick*, 2000]. We produced 30 InSAR images with relatively good coherence over the area of interest (Figure 2 and Table 1). The baselines for these images range from 3 m to 478 m, and the corresponding altitudes of

Table 1. Specifications and Modeling Results for the InSAR Images

Figure	Track	t_0	t_1	Baseline, m	Δt, years	Quadrants	β 10^{-5} m^{-2}	Solution Length, 10^6 m^3	RMSE, 10^{-3} m	Source Strength, s × 10^6 m^3		
										C_1	C_2	C_3
2a	201	Jan. 1993	Aug. 1993	29	0.58	894	40.	1.73	3.7	0.7151	0.0389	0.0181
2b	201	April 1993	Oct. 1993	−186	0.50	712	8.0	1.46	1.8	0.5637	0.0152	0.0131
2c	473	Dec. 1992	May 1993	253	0.41	697	2.0	1.77	1.0	0.8168	0.0062	0.01507
2d	473	June 1993	June 1995	45	2.00	646	3.0	1.30	1.2	0.1979	−0.1004	−0.0265
2e	201	June 1993	Sept. 1995	143	2.25	641	5.0	1.19	2.0	0.0862	−0.0748	−0.0316
2f	473	June 1993	Aug. 2000	169	7.25	755	1.0	3.08	2.4	1.2534	−0.3040	−0.0006
2g	201	Aug. 1993	May 1995	−93	1.75	1038	4.0	1.89	1.4	0.0788	−0.1574	−0.0387
2h	201	Aug. 1993	Sept. 1997	154	4.09	1113	4.0	1.87	3.0	0.0323	−0.2189	−0.0557
2i	201	Aug. 1993	Sept. 1999	157	6.09	1163	2.0	3.13	2.8	0.7702	−0.3140	−0.0425
2j	201	Aug. 1993	Sept. 2000	168	7.09	1246	1.0	3.40	2.8	0.7368	−0.3315	−0.0006
2k	201	Sept. 1993	Sept. 1997	−418	3.91	1105	2.0	2.23	2.9	0.1716	−0.1954	−0.0405
2l	201	Sept. 1993	Oct. 1998	36	5.08	1228	2.0	2.59	2.6	0.0337	−0.2596	−0.0706
2m	201	July 1993	Sept. 1995	201	2.17	933	3.0	1.62	1.8	0.0590	−0.1104	−0.0385
2n	201	May 1995	Sept. 1997	246	2.34	519	6.0	0.89	2.0	0.0267	−0.0438	−0.0207
2o	473	June 1995	Sept. 1999	−346	4.24	768	0.8	2.13	1.9	0.5961	−0.2151	−0.0427
2p	473	June 1995	Aug. 2000	123	5.16	682	1.0	2.65	2.1	1.1349	−0.2524	0.00839
2q	201	Sept. 1995	July 2000	−101	4.83	829	2.0	2.55	2.9	0.8577	−0.2327	−0.0150
2r	201	Sept. 1997	Sept. 1999	3	2.00	907	7.0	1.60	1.9	0.5644	−0.1128	0.0047
2s	201	Sept. 1997	Sept. 2000	14	3.00	1215	2.0	2.72	1.9	1.3201	−0.1270	−.00067
2t	201	Oct. 1997	Oct. 1998	478	1.00	562	10.	0.50	1.4	−0.0485	−0.0277	−0.0099
2u	201	Oct. 1997	Sept. 1999	27	1.92	615	8.0	1.21	1.6	0.5247	−0.0693	0.0046
2v	201	Oct. 1998	Sept. 1999	−450	0.92	764	7.0	1.67	1.7	0.6515	−0.0441	0.0083
2w	201	Oct. 1998	Sept. 2000	−439	1.92	965	10.	3.04	1.7	1.3217	−0.0434	0.0091
2x	201	July 1999	Sept. 1999	−47	0.17	576	8.0	0.82	0.7	0.1527	−0.0292	0.0019
2y	473	July 1999	Aug. 2000	−435	1.08	788	10.	2.05	2.7	0.9224	−0.0193	0.0179
2z	201	July 1999	Sept. 2000	−36	1.17	977	2.0	2.43	1.1	1.0836	−0.0377	0.0070
2aa	473	Sept. 1999	July 2000	−118	0.83	955	2.0	2.23	1.2	0.8841	−0.0427	0.0061
2bb	473	Sept. 1999	Aug. 2000	469	0.91	846	1.0	2.02	1.3	0.9779	−0.0349	0.0115
2cc	201	Sept. 1999	Sept. 2000	11	1.00	869	4.0	1.87	1.2	0.9037	0.0058	0.0080
2dd	473	Oct. 1999	July 2000	71	0.75	822	1.0	1.62	0.8	0.5527	−0.0156	0.0004

ambiguity, h_a, range from 3203 m to 22 m. For these inteferograms, removing the topographic contribution with a DEM of 10-m systematic vertical error could cause a phase error of less than 0.5 of a fringe [e.g., *Massonnet and Feigl*, 1998].

[10] Twenty-one of the images are constructed from track 201 scenes and the other nine images are constructed from track 473 scenes. The line-of-sight (LOS) vectors are [0.416, −0.097, 0.904] and [0.362, −0.084, 0.928] for tracks 201 and 473, respectively. Some of the intervals are confined to the 1992–1993 eruption, some span the coeruption and posteruption intervals, and some are limited to posteruption intervals (Table 1). None of the images are derived from scenes predating the onset of the 1992 eruption. The first image of Seguam Island, from the ERS-1 satellite, was collected on 30 December 1992, 3 days after the onset of the most recent eruption.

[11] In general, Seguam Island maintains higher interferometric coherence over longer time periods than other Aleutian volcanoes [*Lu et al.*, 2003b, and references therein]. For example, the 6-year InSAR image (Figure 2i) is coherent over most of the island, perhaps because the percentage of blocky lava covering Seguam Island is higher than that for other Aleutian islands (J. Power, personal communication, 2000). The eastern portion of the island is vegetated and normally not coherent for multiyear InSAR images. Surprisingly, we produced a few coherent InSAR images that use images acquired in December 1992, January 1993, and April 1993 (Figures 2a, 2b, and 2c). However, the February–March 1993 images are not coherent, most likely due to relatively thick snow and ice coverage.

[12] The InSAR images confined to the 1992–1993 eruption are characterized by a relatively broad and oblong pattern of deformation toward the satellite (i.e., uplift) that is roughly centered on the eastern (historically inactive) caldera and elongated along the long axis of Seguam Island. Deformation during the first few years following the eruption is dominated by two separate regions roughly centered on the east and west calderas, respectively, and the displacement is generally away from the satellite (i.e., subsidence). During the later posteruption intervals, the pattern of subsidence near Pyre Peak persists, while the other deformation center on the eastern caldera changes from subsidence to uplift. During these later intervals, the broad uplift deformation pattern centered on the eastern caldera reemerges. The details of the transient deformation, and therefore the transient deformation source behavior determined from the 30 images individually, are difficult to ascertain. However, when combined with innovational modeling, the deformational data set that is rich in spatial and temporal complexity gives us an opportunity to view the transient, dynamic processes at work within Seguam Island.

3.2. Reduction: Quadtree Algorithm

[13] Each of the 30 InSAR images includes more than 10^5 coherent pixels. We reduce the number of pixels in each image using a quadtree algorithm [*Samet and Webber*, 1988] to accommodate computational requirements of the modeling. In our application, this process reduces the number of data by about two orders of magnitude, depending on the characteristics of each InSAR image. Each image

is padded into a square array having 2^n pixels per side, where n is a positive integer. The image is divided into quadrants and subquadrants until the data in a quadrant satisfy three criteria: (1) the number of coherent pixels in a quadrant must be equal to or greater than a specified fraction of the total number of pixels, (2) the variance of the coherent pixels must be less than or equal to a specified criterion, and (3) the size of a quadrant side must be equal to or greater than a specified number of pixels.

[14] We chose 0.9 for the minimum ratio of coherent to total pixels in a quadrant. By allowing some pixels to be incoherent (a minimum ratio less than 1.0), we can avoid subdividing a quadrant that contains a few incoherent pixels, but satisfies the two other constraints.

[15] The second criterion represents the maximum variability of pixel values within a quadrant. The standard deviation of pixel values must be less than or equal to 3.0 mm. Though somewhat subjective, this value is near the low end of ERS-1/ERS-2 InSAR deformation resolution [e.g., *Zebker et al.*, 1994] and provides reasonable approximations of the parent images. If the standard deviation is lowered, the number of quadrants increases and the reduced image matches the parent image better. However, a specified variability substantially less than the deformation resolution of InSAR imagery increases the number of quadrants without increasing the amount of useful information. If the criterion is substantially increased, the reduced image no longer resembles the parent image.

[16] The third criterion reduces the number of quadrants required for irregular boundaries in the InSAR images, which are problematic for the incremental (2^{2n} pixel) quadrant sizes. For example, a boundary between major coherent and incoherent regions, such as a coastline with an azimuth of 45°, requires an individual quadrant for each coherent pixel. In this case, the next larger size quadrant (2×2 pixels) contains one incoherent pixel and does not satisfy the first constraint. The third criterion requires quadrants having at least 4×4 coherent pixels and effectively removes pixels in problematic boundary areas.

4. Deformation Models

[17] A variety of source mechanisms have been proposed to account for volcano deformation, including magma intrusion and withdrawal [*Mogi*, 1958], thermoelastic contraction [*Fialko and Simons*, 2000], and poroelastic effects [*Lu et al.*, 2002]. For computational efficiency, these source mechanisms are typically assigned simple geometries (e.g., point, tabular, disk, and triaxial ellipsoid). Using the InSAR deformation shown in Figure 2i as an example, we illustrate the limitations of assigning a priori simple deformation sources. The deformation pattern in this image is dominated by two roughly circular areas centered on the east and west calderas, respectively (Figure 3). We attempt to account for this deformation by simultaneously fitting two dilatational point sources to the InSAR image.

[18] The forward solution for displacement, u, at point x on the free surface of a homogeneous isotropic elastic half-space (HIEHS) caused by a dilatational point source, with location ξ, is

$$u_m(x_1, x_2, 0) = s\, u^*_m, \tag{1}$$

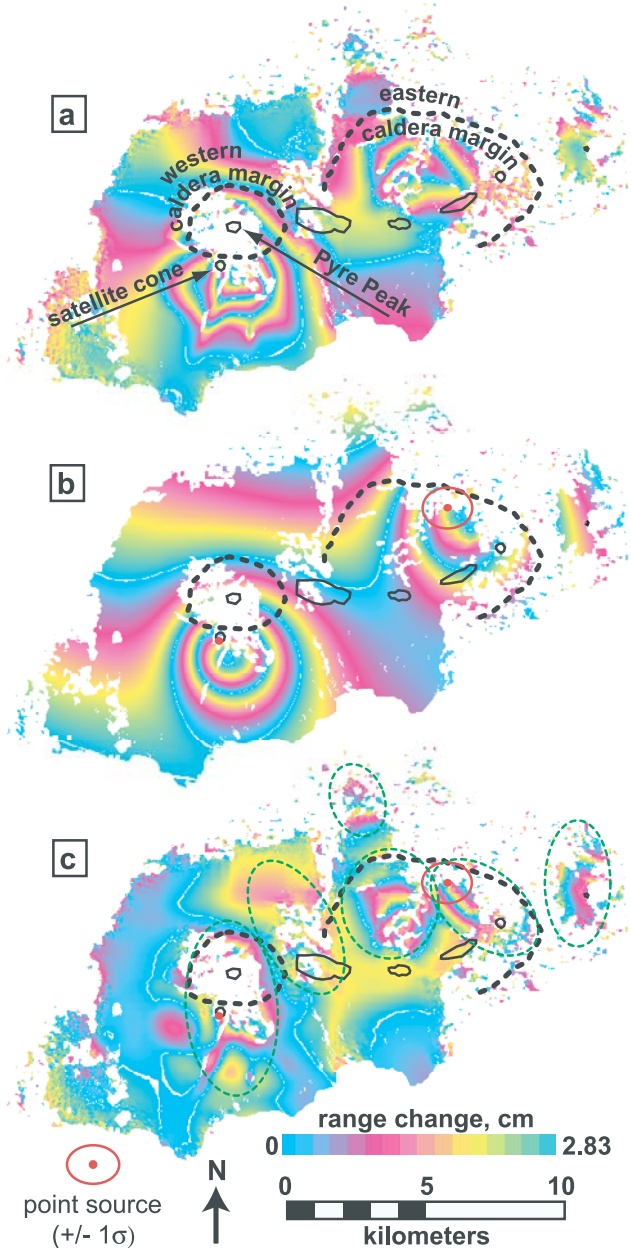

Figure 3. Standard modeling approach. An a priori deformation model consisting of two point sources is chosen to account for the two roughly circular regions of deformation suggested by the InSAR image shown in Figure 2i. Caldera boundaries and vents are shown for spatial reference. (a) InSAR image. (b) Predicted InSAR image using the two best fit point sources. (c) Residual. The six regions (enclosed in the dashed green ellipses) having at least one fringe of misfit illustrate the failure of the standard approach using a priori point source models.

where

$$u^*_m = \frac{(x_m - \xi_m)}{\left[(x_1 - \xi_1)^2 + (x_2 - \xi_2)^2 + (-\xi_3)^2\right]^{3/2}}$$

for coordinate indices m = 1, 2, and 3. The predicted displacement at the free surface is thus a linear function of

Table 2. Parameters for Two Point Source Deformation Model[a]

Parameter	Western Source	Eastern Source
s, m^3	−370,000 ± 60,000	−900,000 ± 600,000
x,[b] m	9,330 ± 80	17,900 ± 900
y,[b] m	−14,400 ± 100	−9,400 ± 700
d, m bsl	1,400 ± 300	2,600 ± 800

[a]RMSE (1σ), 0.007 m.
[b]With respect to the top-left corner of the InSAR images (UTM zone 2, X = 387,116 m, Y = 5,809,595 m).

the source strength, s. Following the method of *Lu et al.* [2003a], we use the downhill simplex method and Monte Carlo simulations [*Press et al.*, 1992] to estimate optimal source parameters and uncertainties (Table 2) for both point sources based on the root-mean square-error (RMSE) between the predicted and actual InSAR image. Although the fit appears to be sufficient based on the RMSE ≈ 7 mm, the residual contains at least six different areas having systematic errors of at least one fringe. The small RMSE is due to the majority of data lying outside the two regions that dominate the deformational pattern [*Lundgren and Rosen*, 2003]. We could attempt to fit the InSAR image using several additional a priori sources simultaneously with the two point sources, but it is readily apparent that the deformation source solution quickly becomes ambiguous. This problem would be amplified when applied to the 30 separate InSAR images that are available for Seguam island. The failure of the standard method using a priori deformation sources is no surprise. A careful visual inspection of the InSAR deformation pattern reveals that although the deformation of the two circular regions dominates the InSAR image, the deformation patterns within these two regions are not radially symmetric. Hence the assumed model using two point sources fails.

[19] Rather than pursue an ad hoc trial and error approach using point, dike, and sill sources, we assume neither a simple combination of simple source geometries nor an a priori deformation source mechanism to account for the spatial and temporal complexities observed in the 30 InSAR images of Seguam Island. The relationship given in equation (1) is valid for point source approximations caused by changes in the volume (ΔV_m) of and pressure (ΔP_m) in a magma chamber [*Lu et al.*, 2002]. The point source relationship is also valid for incremental changes in pore fluid pressure (ΔP_f) in a confined aquifer as well as for the analogous case of thermoelastic deformation caused by incremental changes in temperature (ΔT) in a volume of rock:

Magma injection

$$s = \Delta P_m (1-\nu)\frac{r^3}{G} = \Delta V_m \frac{(1-\nu)(1+\nu)}{2\pi(1-2\nu)}, \qquad (2a)$$

Table 3. Material Properties

Property	Value
ν[a]	0.27
G[a]	1.9×10^{10} Pa
c_f[a]	4.5×10^{-12} Pa^{-1}
α_t[b]	1.0×10^{-5}°K^{-1}

[a]From *Wang* [2000].
[b]*Turcotte and Schubert* [1982].

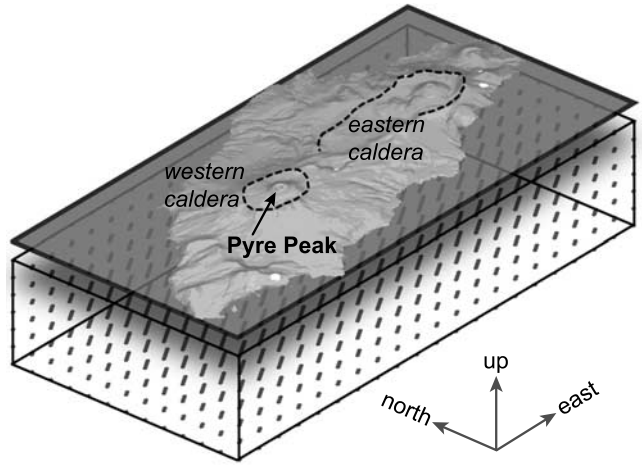

Figure 4. Deformation point source array. The seven-layer, three-dimensional array of point source nodes is horizontally centered on Seguam Island. Each layer is a 23 × 15 two-dimensional array of nodes aligned with the east and north directions, respectively. The entire array extends from 500 to 7500 m below sea level (bsl). Node spacing is 1 km in all directions. Dashed lines outline the two caldera margins.

Poroelastic contraction

$$s = \Delta P_f V_f \frac{c_f(1-\nu)}{\pi}, \qquad (2b)$$

Thermoelastic contraction

$$s = \Delta T V_t \frac{\alpha_t(1-\nu)}{\pi}, \qquad (2c)$$

where ν is Poisson's ratio, G is the shear modulus, r is the radius of the chamber, V_f is the volume of the aquifer, c_f is Geertsma's uniaxial poroelastic expansion coefficient [*Wang*, 2000], V_t is the volume of the rock experiencing the temperature change, and α_t is a coefficient of linear thermal expansion equivalent to one third of the volumetric thermal expansion coefficient [*Nowacki*, 1986].

[20] We develop a source cluster method that consists of a relatively dense three-dimensional array of potential point sources (nodes) [*Mossop and Segall*, 1999; *Vasco et al.*, 2002]. Rather than impose idealized a priori source geometries, finite clusters of nodes assume amorphous shapes dictated by the data. The three-dimensional array of nodes has seven layers that are horizontally centered on Seguam Island. Each layer is a 23 × 15 two-dimensional array of nodes aligned with the east and north directions, respectively (Figure 4). The array extends from 500 to 7500 m below sea level (bsl), and node spacing is 1 km in all directions, in accord with *Mossop and Segall* [1999] and *Vasco et al.* [2002]. We assume all deformation is caused by sources at depths of 500–7500 m. An implication of this assumption is that we neglect very shallow processes having small deformational wavelengths, such as the thermoelastic contraction of the 1992–1993 lava flow. Furthermore, the small horizontal dimensions of the island and spatial extent of the InSAR data severely limit the resolution of potential sources at depths beneath the node array. The HIEHS assumptions implicit to equation (1) most likely do not represent the

actual field situation very well. Rigorous assessments of the assumptions require numerical methods and are not performed in this study.

[21] The forward solution for a distribution of displacements at the free surface of an HIEHS, caused by a distribution of dilatational point sources, is the superposition of the displacement distributions contributed by each of the sources

$$\mathbf{Gs} = \mathbf{d}, \tag{3}$$

where $\mathbf{G}$ is a matrix of Green's functions for displacement, $\mathbf{s}$ is a vector of dilatational source strengths, and $\mathbf{d}$ is a vector of observed displacements. We do not, at this point, need to specify any of the source mechanisms in equation (2). Each component of the Green's function matrix, $\mathbf{G}_{ij}$, is the predicted displacement for location j caused by a unit dilatational point source i. For the HIEHS model used in this analysis, the relationship is the projection of u^* onto the LOS vector for a corresponding InSAR data vector. The predicted displacements are corrected for topographic effects [*Williams and Wadge*, 1998].

[22] The relationship in equation (3) is appended to a form that includes constraints to minimize the roughness of the three-dimensional source strength distribution. We solve for the source distribution using a damped least squares (DLS) method that includes Laplacian smoothing [*Freymueller et al.*, 1994] and allows us to easily control solution roughness and impose dilatational boundary conditions on the three-dimensional source array. The a priori weighting matrix, $\mathbf{w}$, normalizes and weights the data in proportion to the number of pixels in each quadrant of a reduced InSAR image. The forward solution then takes the form

$$\hat{\mathbf{G}}\,\hat{\mathbf{s}} = \hat{\mathbf{d}}, \tag{4}$$

where

$$\hat{\mathbf{G}} = \begin{pmatrix} \mathbf{w}^{-1}\mathbf{G} & \mathbf{xy1} \\ \beta\mathbf{L} & \mathbf{000} \end{pmatrix}, \quad \hat{\mathbf{s}} = \begin{pmatrix} \mathbf{s} \\ \mathrm{a} \\ \mathrm{b} \\ \mathrm{c} \end{pmatrix}, \quad \hat{\mathbf{d}} = \begin{pmatrix} \mathbf{w}^{-1}\mathbf{d} \\ \mathbf{0} \end{pmatrix},$$

where $\mathbf{L}$ is a Laplacian operator and β is an adjustable damping parameter that controls the relative importance of fitting the data versus minimizing the roughness of the solution. The relationship is further conditioned to account for phase ramping in the InSAR images by simultaneously fitting a plane. Column vectors corresponding to the centroidal positions of the quadrants and a unity vector are included in $\hat{\mathbf{G}}$. The coefficients for a plane $a\mathbf{x} + b\mathbf{y} + c$ are appended to the source vector.

[23] The Laplacian operator is implemented with the finite difference approximation [*Wang and Anderson*, 1982] for $\mathbf{s}$, recast into a three-dimensional array, $\mathbf{s}^*$

$$\nabla^2\mathbf{s}^* = 0 \cong \frac{\mathbf{s}^*_{i-1,j,k} - 2\mathbf{s}^*_{i,j,k} + \mathbf{s}^*_{i+1,j,k}}{(\Delta x)^2} + \frac{\mathbf{s}^*_{i,j-1,k} - 2\mathbf{s}^*_{i,j,k} + \mathbf{s}^*_{i,j+1,k}}{(\Delta y)^2} + \frac{\mathbf{s}^*_{i,j,k-1} - 2\mathbf{s}^*_{i,j,k} + \mathbf{s}^*_{i,j,k+1}}{(\Delta z)^2}, \tag{5}$$

where Δx, Δy, and Δz represent the three-dimensional node spacing. The matrix $\mathbf{L}$ is constructed such that the *nth* row in $\mathbf{L}$ contains source component coefficients in equation (5) for columns corresponding to the appropriate source

$$L^n = \begin{cases} L^n_{(k-1)nl+(j-1)nc+i} = -2\left[(\Delta x)^{-2} + (\Delta y)^{-2} + (\Delta z)^{-2}\right] \\ L^n_{(k-1)nl+(j-1)nc+(i-1)} = (\Delta x)^{-2} \\ L^n_{(k-1)nl+(j-1)nc+(i+1)} = (\Delta x)^{-2} \\ L^n_{(k-1)nl+(j-2)nc+i} = (\Delta y)^{-2} \\ L^n_{(k-1)nl+(j)nc+i} = (\Delta y)^{-2} \\ L^n_{(k-2)nl+(j-1)nc+i} = (\Delta z)^{-2} \\ L^n_{(k)nl+(j-1)nc+i} = (\Delta z)^{-2} \end{cases}, \tag{6}$$

where L^n is the nth row vector of $\mathbf{L}$ and subscripts nc and nl are the number of columns and layers, respectively, of the three-dimensional node matrix. We assume no sources outside of the three-dimensional node array and apply Dirichlet-type boundary conditions [*Wang and Anderson*, 1982] to $\mathbf{s}^*$.

5. Results

[24] We estimate a family of source distributions for each of the 30 InSAR images by inverting equation (4) and sweeping through a range of damping values. The preferred solution for each image is a compromise between fitting the data versus minimizing the solution roughness and satisfying the boundary conditions (Figure 5). We visually identify points of diminishing returns for reducing misfit at the expense of increasing the roughness. We chose not to implement a more rigorous assessment to identify the preferred damping values for two reasons. First, we performed numerous sensitivity analyses and found that small variations in β have little effect on the overall results. Second, statistical assessments, such as the cross validation sum of squares, can lead to unrealistic results [*Freymueller et al.*, 1994]. Preferred damping values range over more than an order of magnitude, from $\beta = 1.0 \times 10^{-5}$ m^{-2} to $\beta = 4.0 \times 10^{-4}$ m^{-2}, suggesting the deformation signals contain substantial variations over time.

[25] A precursory analysis of the preferred solutions suggests three different sources are dominant, although not all three sources appear in all solutions. This is compatible with the visual assessment of the InSAR images discussed in section 3.1. A relatively broad expansion source occurs in the solutions for the coeruptive images (Figures 6a and 7a). This source is roughly centered beneath the historically inactive eastern caldera, however it includes a lobe that extends to the southwest and beneath the Pyre Peak caldera. Immediately following the eruption this source diminished and two relatively local contracting sources emerge beneath the satellite cone southwest of Pyre Peak and the eastern caldera, respectively (Figures 6b and 7b). During 1999–2000 the local contracting source

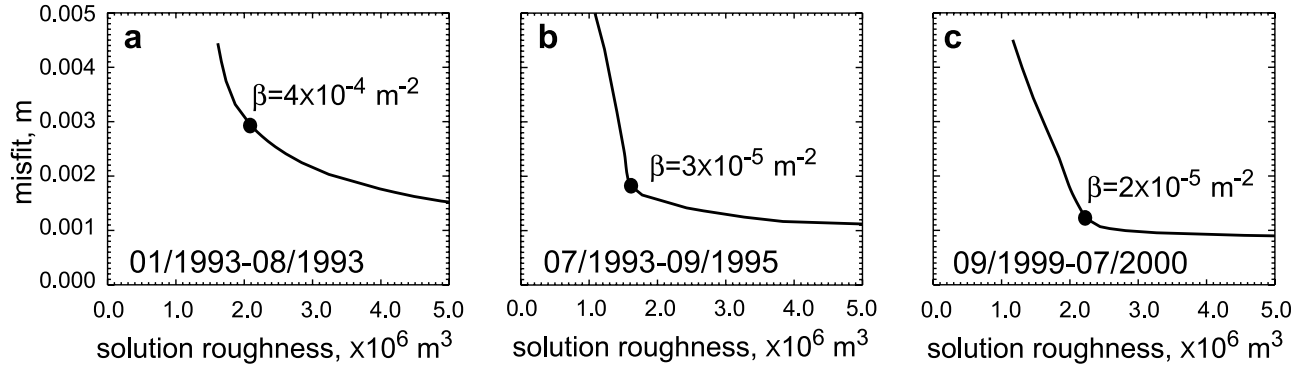

Figure 5. Misfit versus roughness. The model inversion process yields a family of solutions for each of the 30 InSAR images. Three examples illustrating the trade-off between misfit (RMSE) and roughness (where roughness is expressed as solution length, $\Sigma|s|$) are shown for (a) coeruption, (b) early posteruption, and (c) late posteruption intervals. Optimal solutions, shown with the solid circles, attempt to minimize the misfit without significantly increasing solution length. Stated another way, a solid circle identifies the point of diminishing returns from reducing the misfit at the expense of increased solution length.

beneath the Pyre Peak caldera persists and the other contracting source beneath the eastern caldera becomes an expanding source (Figures 6c and 7c). The precise timing of these events is difficult to determine from the solutions derived for the individual images.

5.1. Collective Surfaces

[26] The results of the DLS inversion identify the dominant source features required to predict the deformation shown in each InSAR image. Some of the InSAR images require distinctive source features to predict atmospheric anomalies that contaminate the observed deformation. Collective surfaces, which contain source clusters common to the solutions to all images, allow us to study the transient behavior of the relatively few dominant source features common to all intervals sampled with InSAR.

[27] We use a three-step approach to design collective surfaces containing dominant clusters from the source strength distributions determined for the individual images. First, we sum (stack) the source strength of the corresponding nodes determined from each InSAR image. In this step, systematically dominant sources are amplified while sources that do not make systematic deformation contributions (primarily caused by atmospheric delay anomalies) are reduced. Second, the magnitudes of the stacked sources are normalized for each InSAR interval. Third, collective surfaces enclose clusters of nodes having magnitudes greater than $1/e$ (gray areas in Figure 6). The somewhat arbitrary $1/e$ cutoff retains the robust features of the source clusters identified using the DLS method, and small variations from this cutoff had little effect on the overall prediction characteristics. The source contributions from the nodes within the each of the collective surfaces are retained and those outside of the collective surfaces are discarded. The collective surfaces spatially contain about 15 percent of the node array. The total magnitude of the source array contained within the collective surfaces ranges from 30 to 54 percent, depending on the particular solution.

[28] Three distinct clusters, in agreement with the precursory source cluster analysis and visual inspection of the InSAR images, are spatially identified in Figure 8. The first cluster, C_1, ranges in depth from 500–5500 m bsl, has an apparent volume of 335 km^3, and represents an expanding source extending beneath both calderas. The second cluster, C_2, has an apparent volume of 32 km^3 and is a shallow, predominantly contracting source extending from 500–3500 m bsl. This cluster is roughly centered beneath the satellite cone to the southwest of Pyre Peak. The third cluster, C_3, has an apparent volume of 5 km^3 and is located beneath the eastern caldera at depths of 500–1500 m bsl. Note that the apparent cluster volumes represent the spatial volumes of the clusters and not the total source strength. Furthermore, nodes in a cluster need not be active all the time.

Figure 6. Deformation source strength distributions. Each solution for the 30 images is a three-dimensional distribution of source strength. Expanding (positive) and contracting (negative) sources are shown in red and blue, respectively. Horizontal slices of three examples of source strength distributions, corresponding to the misfit versus solution length examples in Figure 5, are shown for (a) coeruption, (b) early posteruption, and (c) late posteruption intervals. The coeruptive source strength distribution is a large, single cluster of expanding nodes. The early posteruption distribution is dominated by two relatively local contracting clusters centered beneath the two calderas. The late posteruption distribution is dominated by a large cluster of expanding nodes similar to that of the coeruption interval. However, the contracting cluster beneath Pyre Peak persists. The contracting cluster in the southeast corner is likely an artifact of atmospheric anomalies because it does not systematically appear in the other late posteruption distributions. The gray shaded regions contain nodes within the collective surfaces discussed in the text. The dark and light gray regions are predominantly contracting and expanding regions, respectively. These gray regions do not exactly match the examples shown because the regions are determined from contributions from all 30 InSAR images.

[29] We did not formulate the problem (4) to account for tropospheric effects. Because the topographic relief over the deformation area is less than 1000 m, the topography-correlated tropospheric fringes should be insignificant [*Beauducel et al.*, 2000; *Wicks et al.*, 2002]. Because the atmospheric artifacts do not correlate in time, if many InSAR images are used to construct the deformation models, the effects of artifacts should partly cancel and the final source models should be relatively free of atmospheric effects. The technique of collective surfaces, which contain

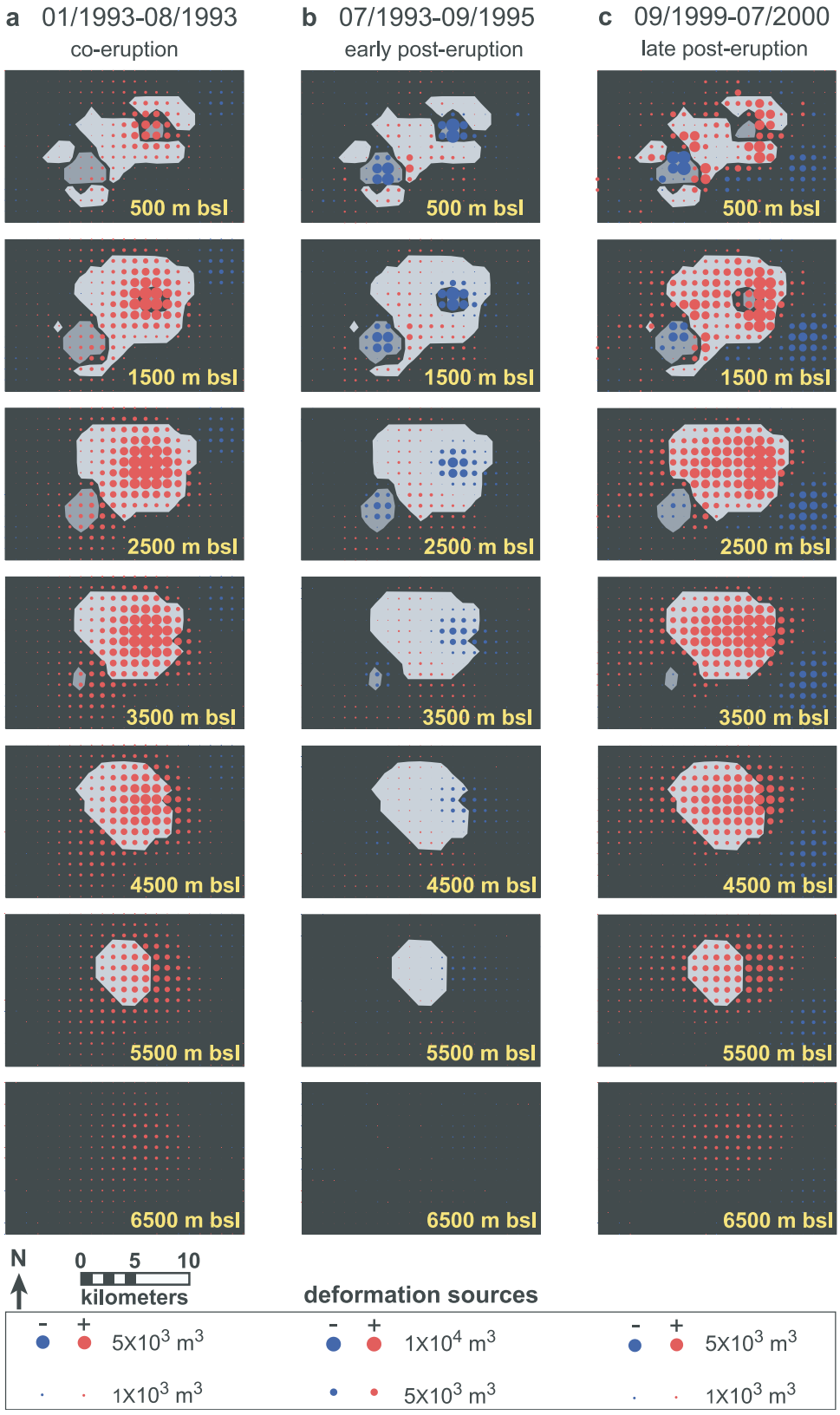

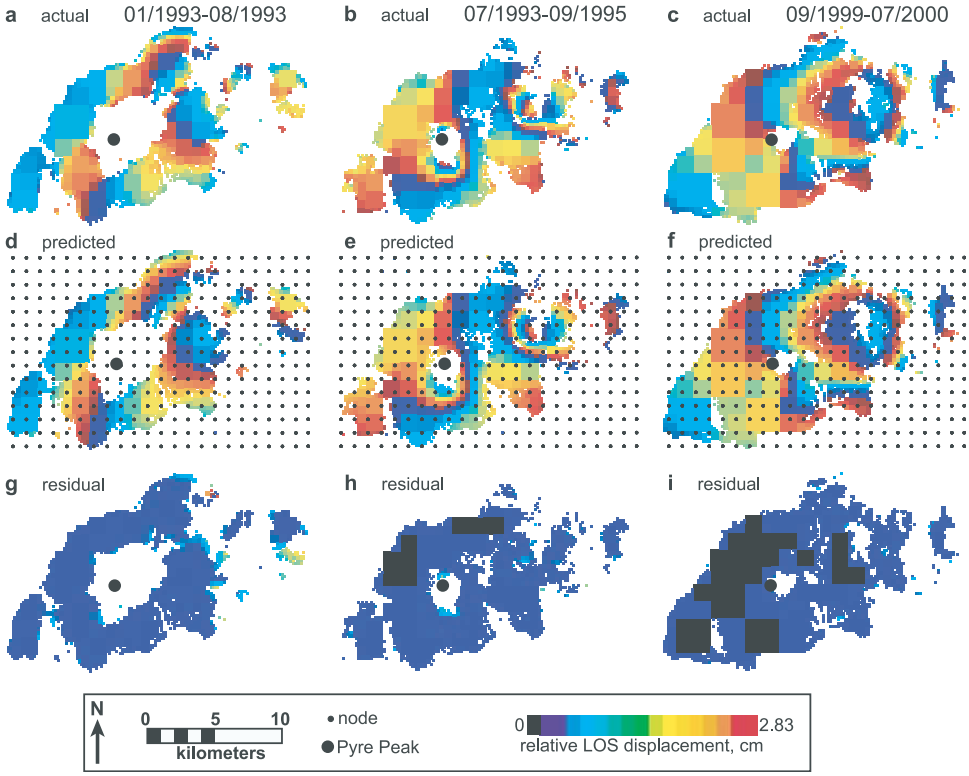

Figure 7. Deformation predictions. Each color cycle, blue-yellow-red, is 2.83 cm of displacement along the LOS vector toward the satellite. (a–c) The reduced actual, (d–f) predicted, and (g–i) residual (difference between actual and predicted deformation) deformations are displayed. The grid in Figures 7d–7f shows the horizontal location of the three-dimensional source-node array. The reduced images (Figures 7a–7c) are derived from the InSAR images using the quadtree algorithm described in the text. These three examples represent the excellent agreement between observed and modeled displacement for all 30 InSAR images.

source clusters common to the solutions to all images, allows us to study the transient behavior of the relatively few dominant source features common to all intervals sampled with InSAR.

5.2. Model Resolution

[30] The model resolution matrix describes how well the estimated source strength parameters of the node array are resolved. The model resolution matrix is a function of the data kernel (**G**), the weighting matrix (**w**), and is independent of the data vector (**d**) [*Menke*, 1989]. The diagonal elements of the model resolution matrix indicate the resolution of the source strength for each node. If the model resolution matrix is an identity matrix, then the estimated source strength for each node is perfectly resolved. The resolution is arbitrarily improved, at the expense of estimated source strength variance, by decreasing the node spacing. However, the relative variations of the diagonal elements of the model resolution matrix reveal where the source strength parameters are best resolved.

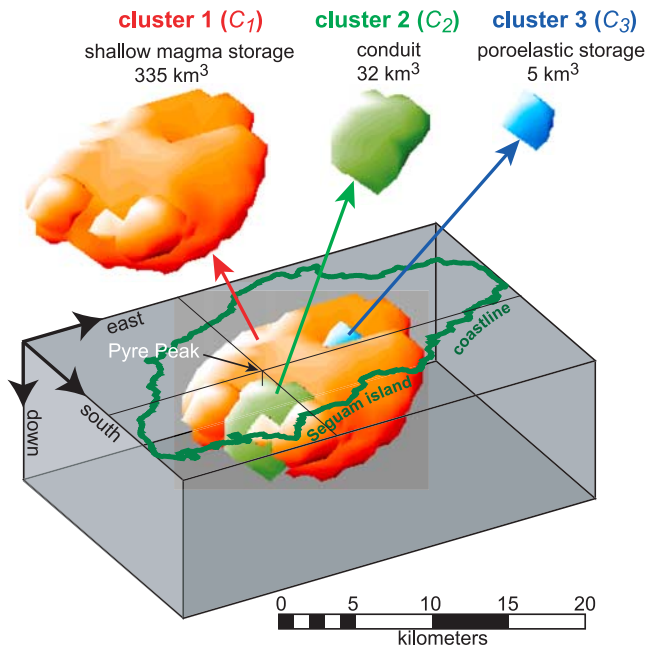

Figure 8. Deformation source clusters. The collective surfaces identify clusters containing normalized sums of sources greater than 1/*e*. This method produces three dominant source clusters. The broad, flattened shape of cluster 1 is most likely a distortion of the true shape of the deformation source because it is not compensated for the actual heterogeneous elastic material properties. Furthermore, the distortion may be aggravated by deformation contributions from a deeper source that we did not account for.

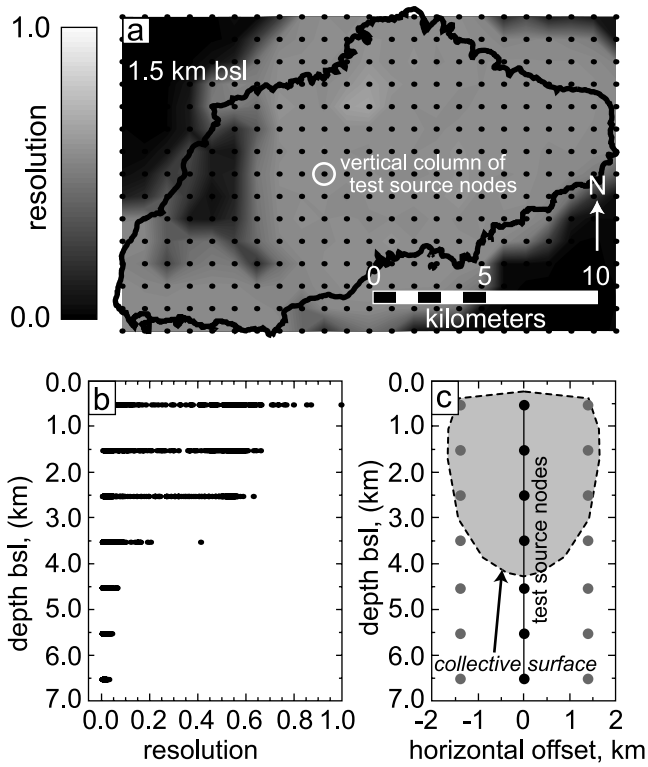

Figure 9. Model resolution. (a) Normalized diagonal elements of the model resolution matrix for the nodes having a depth of 1.5 km bsl. The thick black line outlines the coast of Seguam Island. The solid circles are the horizontal positions of the source nodes. Nodes within or near the coastline have relatively higher resolution than those offshore. The low resolution beneath the western part the island is due to the sparse distribution of reduced InSAR quadrants (shown in Figure 6c). (b) Normalized diagonal elements of the model resolution matrix as a function of depth. Each layer contains 15 × 23 estimations. Resolution decays as a function of depth, as expected from equation (1). The source strengths of the nodes in the first four layers are relatively well resolved. (c) Resolution test. A constant source strength is applied to the vertical column of test nodes located in Figure 9a. The resulting collective surface, shown in cross section, excludes deep nodes from the actual source (black circles) and includes nonsource (dark gray circles) shallow nodes. Nodes within the light gray region are contained within the collective surface. This suggests the minimum horizontally resolvable features measure about 2 km.

[31] The overall model resolution pattern is as expected (Figure 9). Horizontally, the nodes contained within the onshore footprint have higher resolution than those offshore, because the onshore nodes are generally within the coherent portions of the InSAR image. Vertically, the resolution decays with depth. Source strength parameters are well resolved in the first four layers of nodes. Source strength for nodes beneath about 4 km bsl are poorly resolved (Figure 9b). In spite of the three-dimensional nature of the smoothing constraints given in equation (5), the inverse solution favors shallow sources. This suggests an additional depth-dependent penalty function may be required in equation (4) in future analyses.

[32] To test the spatial resolution of the inverse method, we apply a constant source strength to a vertical column of nodes, roughly horizontally centered on the island (Figure 9a). A synthetic InSAR image is constructed from the superposition of displacement predictions and reduced with the quadtree algorithm discussed in section 3.2. This synthetic data is inverted using the method described above. The inversion recovers the horizontal position of the vertical column of nodes. However, the collective surface is smeared horizontally and contracted upward, such that it includes only nodes from the four shallowest layers (Figure 9c). Because the inverted solution includes a shallower distribution of nodes than in the actual source, only about 30 percent of the source strength is recovered. This resolution test indicates that (1) resolvable horizontal features require a characteristic length of at least 2 km, (2) the collective surfaces are smeared horizontally and bias toward shallow features, and (3) the source strength magnitudes most likely underestimate the actual magnitudes.

5.3. Transient Behavior

[33] Study of the 30 InSAR images (Figure 2) suggests that each of the three clusters (Figure 8) is associated with a distinctive transient behavior. The spatial and temporal characteristics of the clusters may be independent, although intuitively, the behavior among the clusters should be interrelated. The estimated source strength results from the individual InSAR epochs suggest that the rate of change in source strength is not constant for any of the clusters (Figure 10). We test this hypothesis by fitting a constant flux (Q) to the source strength of each cluster for the individual InSAR epochs [e.g., *Lu et al.*, 2003b], using the relationship

$$s_j^{Ci} = (t_{j1} - t_{j0})Q^{Ci}, \tag{7}$$

where s_j^{Ci} is the source strength of cluster i for time epoch j; t_{j0} and t_{j1} are the initial and final times, respectively, of epoch j; and Q^{Ci} is the flux for cluster i. Constant flux temporal models do not adequately characterize the combined coeruptive and posteruptive temporal behavior of any of the clusters (Figure 11). The posteruptive flux of C_1 apparently increases over time and the posteruptive flux of C_3 migrates from decreasing to increasing. However, a constant flux temporal model fits the posteruptive behavior of C_2 reasonably well.

[34] Rather than fit the temporal behavior of the clusters with higher order polynomial functions of time to account for multiple critical points, we generate sequences of regular incremental time series behavior. This process consists of five steps. The lengths of the individual InSAR image epochs range from a few months to more than six years (Figure 10a and Table 1). First, we set the time increment for the regularized time series to 0.25 years, slightly larger than the smallest InSAR image epoch. Second, the bounds of each epoch are either interpolated or extrapolated to the nearest quarterly time increment (Figure 10b). Third, the source magnitude for each cluster is scaled according to the interpolation or extrapolation. Fourth, an average incremental source value during each 0.25-year period is obtained for each cluster from the individual images that

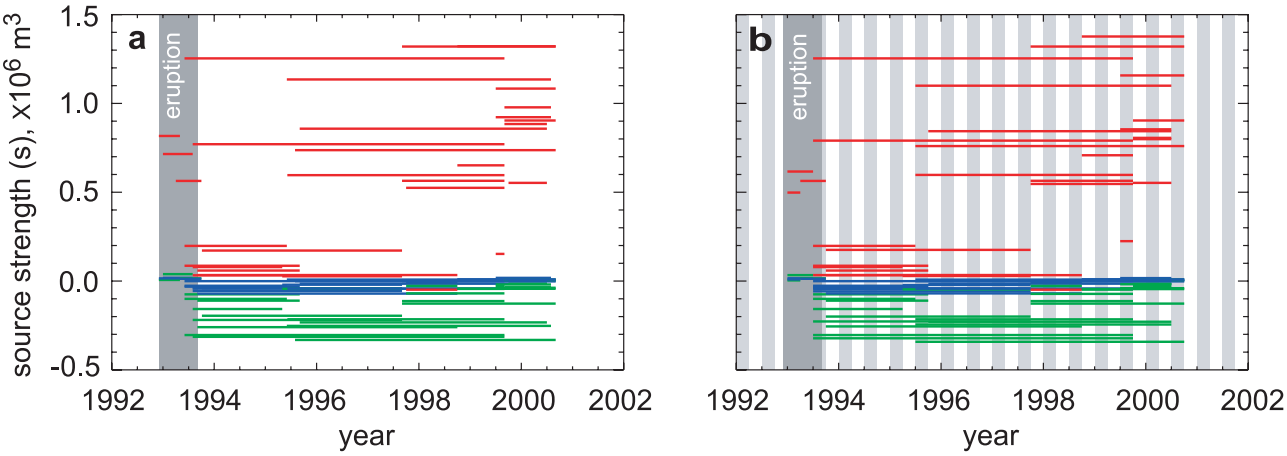

Figure 10. Cluster source strength. The source strength for each cluster is shown for each InSAR epoch. Red, green, and blue bars correspond to cluster 1, cluster 2, and cluster 3, respectively. (a) Actual cluster source strength intervals. (b) Regularized cluster source strength intervals. Time intervals are either interpolated or extrapolated to the nearest quarter. Source strength values are scaled accordingly. Alternating gray and white vertical bars correspond to quarterly time steps.

cover the 0.25-year period. For our data set, the time increment of 0.25 years ensures that each increment will include at least two and as many as 14 source estimations from different InSAR images. Atmospheric anomalies are transient features that are not shared by all InSAR images having different epochs. This fourth step of the time series generation further reduces the influence of false deformation signals caused by atmospheric anomalies. Finally, for each cluster, the average incremental values of source strength for each 0.25-year time step are recursively summed to produce the cumulative source strength as a function of time. This five-step process estimates the regularized time series of source behavior of each cluster (Figure 12).

[35] From Figure 12, we can see that the broad extensional source, C_1, dominates during the 1992–1993 eruption, diminishes during the first few years after the eruption, and becomes predominant again during 1999–2000. The shallow source beneath the Pyre Peak caldera, C_2, expands during the 1992–1993 eruption and then persistently contracts following the eruption. The shallow source beneath the eastern caldera, C_3, expands during the eruption, contracts during the first few years following the eruption, and then begins to expand again in 1999–2000. In general, the source strength of C_1 is approximately 10 times larger than that of C_2, which is in turn 10 times larger than that of C_3 (Figure 12).

6. Discussion

[36] Two models (Figure 13) that combine magma influx, thermoelastic relaxation, and poroelastic effects can account for the transient source cluster behavior, and hence the observed deformation. An overarching caveat for the interpretation of the system's geometry is that the interpretation depends on the applicability of the HIEHS assumptions used in equation (1). If the mechanical system is indeed well represented by an HIEHS, then the collective surface geometry we derive is valid, albeit somewhat distorted by the inverse process, as discussed in section 5.2. Unfortunately, it is unlikely that HIEHS assumptions are truly valid for this

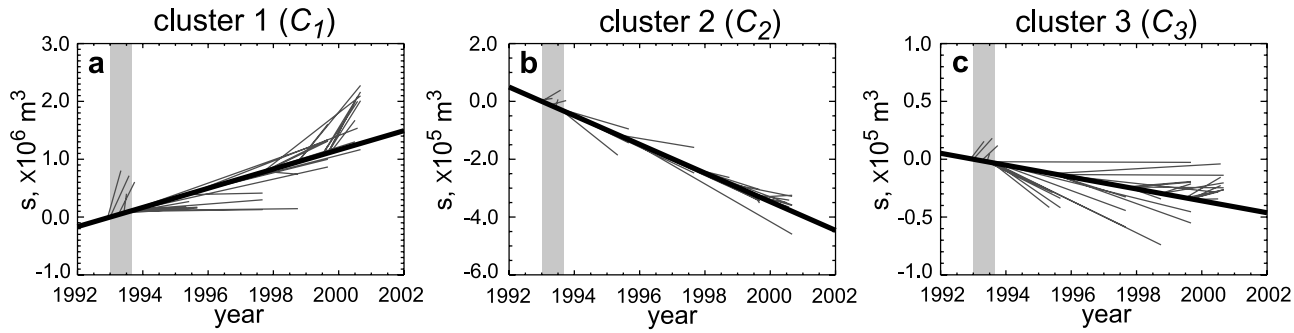

Figure 11. Constant source flux models. Constant source flux models indicate that the transient source cluster behavior cannot be adequately described with linear increases in source strength as a function of time. Thin lines are solutions for individual InSAR epochs. Initial conditions for each epoch are shown with respect to the best fit transient models (thick lines). Gray vertical bars represent the coeruption interval. (a) Cluster 1. (b) Cluster 2. The coeruption behavior is positive, while the posteruption behavior, taken alone, is reasonably approximated with the linear flux model. (c) Cluster 3.

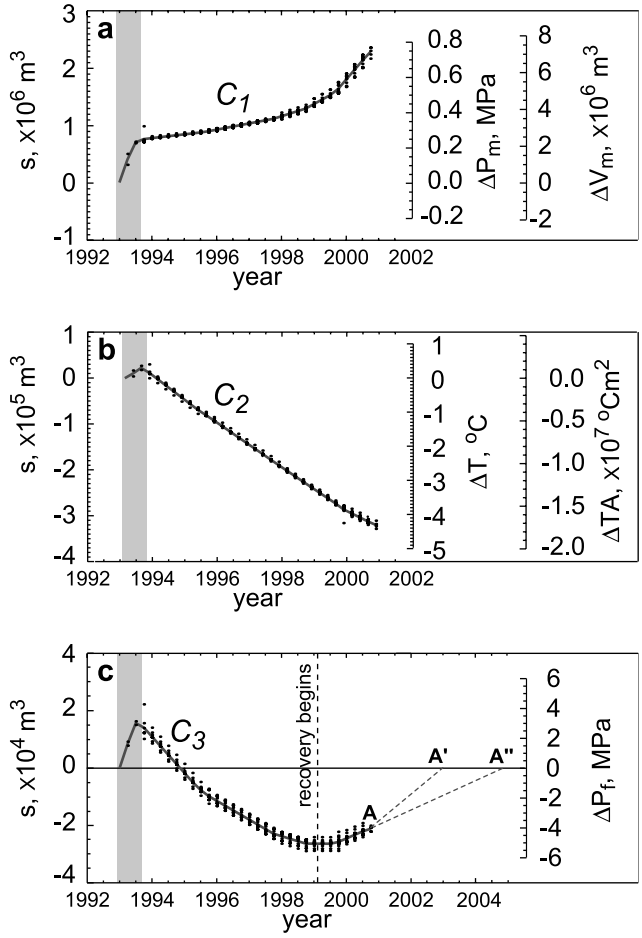

Figure 12. Regularized source strength time series. We generate sequences of regular incremental time series of source strength behavior for each cluster. The thick lines connect the recursively summed average quarterly source strengths. Each vertical "stack" of solid dots represents the quarterly source strength and a recursively summed average value. Elastic constants used to estimate state variables are summarized in Table 3. Scales for equivalent changes in pressure or volume for a magma chamber, temperature of a cooling body, and pore fluid pressure are shown to the right of the plots. (a) Cluster 1. (b) Cluster 2. The magnitudes of ΔT are most likely underestimated because the volume of cluster 2 is grossly overestimated due to our inability to resolve the shape of the conduit. The axis on the far right, ΔTA, assumes the conduit height is 8 km and a horizontal cross-sectional area, A, that combines the conduit and surrounding region of country rock heated during the eruption. (c) Cluster 3. The transient behavior of cluster 3 may provide clues to the timing of the next eruption. If the models discussed in the text are valid, lines A-A′ and A-A″ are bounds on the timing of the next eruption. Because A′ marks the current date, A-A′ is the lower bound on timing. If the rate of dilatation of cluster 3 continues to accelerate, A-A″ is the upper bound on timing of the next eruption.

system and the geometry presented represents an amalgamation of the true source geometry and distortion due to contrasting material properties of the real system and the resolution properties of the inverse method. In addition, the multiple source mechanisms invoked in this study imply a heterogeneous distribution of material properties and arguably preclude the applicability of HIEHS assumptions. Data and associated structural models are available to constrain the subsurface structure of Seguam Island [*Grow*, 1973; *Singer et al.*, 1992b]. However, introducing the additional complexity of a heterogeneous material property distribution requires numerical methods [e.g., *Masterlark*, 2003] and is beyond the scope of this paper.

6.1. Model A

[37] Model A (Figure 13a) is based solely on the InSAR data. Cluster C_1 is interpreted to be a shallow magma storage chamber. Magma flux into this chamber drives the deformational system of Seguam Island and some of this magma makes its way to the surface via a conduit (C_2). A portion of the magma must remain in storage within C_1, because the source strength does not decrease during the eruption interval. Magma influx diminishes during the first few years following the eruption. Sometime around 1999, magma influx increases. Throughout 1992–2000, the source strength is positive in C_1, indicating the pressure was continuously increasing (at variable rates). This continuing increase in pressure suggests the historic eruptions of the volcano may be minor events compared to a much larger, caldera-forming future eruption.

[38] Cluster C_2 is inferred to be the conduit that transports magma from C_1 to the surface. Some of the magma remains stored in C_2, based on the positive increase in source strength during the eruption. Following the eruption, the conduit undergoes thermoelastic contraction as the unerupted magma cools.

[39] Cluster C_3 is a shallow poroelastic storage chamber. During the eruption, pore fluid pressure within this chamber increases due to fluid mass and thermal influx from the degassing magma storage chamber (C_1). During the first few years following the eruption, the pore fluid pressure decays via fluid flow processes. Pore fluid pressure recovery begins during 1999, in response to the accelerated magma influx into the surrounding magma storage chamber (C_1). Cluster C_3 can be interpreted as a pressure gauge for fluid accumulation from degassing magma. As such, the transient behavior of C_3 may provide clues to the timing of the next eruption (Figure 12c). Not all fluids from the spatially expansive degassing magma storage chamber (C_1) are migrating to the relatively localized poroelastic storage chamber (C_3). However, there may be some structure associated with C_3 that favors some combination of fluid migration and entrapment.

6.2. Model B

[40] Model B (Figure 13b) is an alternative interpretation of the spatial and temporal behavior of the clusters using the magmatic system model suggested by *Singer et al.* [1992b]. This system is driven by basaltic magma pulses that deliver magma into a deep storage chamber residing in the lower crust and beneath the node array. A portion of this magma is directly transported to the surface via a conduit roughly centered beneath the satellite cone to the southwest of Pyre Peak. Petrologic evidence indicates these erupted lavas are derived from magma that had very little interaction with the country rock [*Singer et al.*, 1992a, 1993b]. In addition,

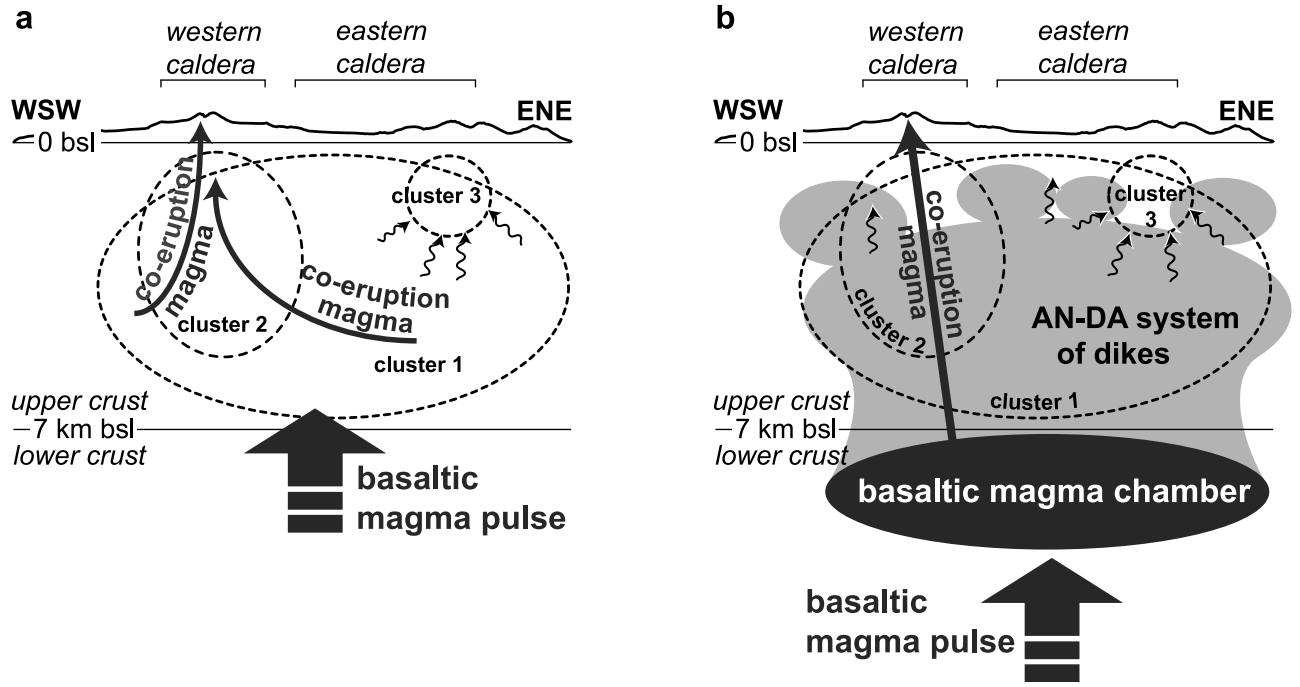

Figure 13. Deformational systems of Seguam Island. WSW-ENE trending cross sections display the schematic magmatic systems of the two proposed models discussed in the text (vertical exaggeration is 4). Sinusoidal arrows represent the products of the degassing magma. (a) Model A. The magmatic system, based on InSAR data alone, is driven by magma influx into cluster 1 (shallow storage). A portion of the magma migrates to the surface via cluster 2 (magma-surface conduit). As the magma in shallow storage degasses, a significant portion of the fluids accumulate in cluster 3 (poroelastic storage). (b) Model B. This magmatic system integrates the InSAR-derived cluster behavior into the model, based on petrologic data, proposed earlier by *Singer et al.* [1992b]. A simplified version of the subsurface structure is shown here. Cluster 1 represents the intrusion into an andesite-dacite (AN-DA) system of dikes. A substantial portion of the degassed fluids from these dikes migrates into cluster 3 (shallow poroelastic storage). Cluster 2 is a direct conduit between a deeper magma source and the surface. Cluster 2 is not directly coupled to cluster 1, as is the case in model A. We cannot image the deep magma source because InSAR spatial coverage is limited to onshore areas, thus restricting our depth resolution.

plagioclase zoning observed in the extruded basalt suggests rapid decompression of basaltic magma due to efficient transport to the surface from depth [*Singer and Pearce*, 1993; *Singer et al.*, 1993]. This direct transport of magma to the surface is also consistent with the extensional regime of the region. Cluster C_2 represents the conduit connecting the storage chamber in the lower crust to the surface of the island. A small amount of magma remains in storage following the eruption and the resulting thermoelastic contraction of C_2 (Figure 12b) represents the cooling of this remaining magma as well as the volume of country rock heated by the transported magma during the eruption.

[41] Magma from the deep storage system is also injected into the upper crust. Cluster C_1 represents this storage space, which we interpret as a system of dikes. This cluster is elongated roughly parallel to the line of vents (Figure 1). The system of dikes permeates the highly fractured shallow subsurface, where andesite and dacite magmas undergo a closed system evolution with little mixing, convection, or rapid decompression [*Singer and Pearce*, 1993]. The residence time of the magma is much greater in C_1 than in the conduit (C_2). In this system of dikes and highly fractured country rock (C_1), the magma degassing process is efficient such that the viscosity and density of the magma increase dramatically and vertical magma transportation stalls at relatively shallow depths [*Spera*, 2000]. Large residence times also allow for the magma differentiation required to produce silicic lavas observed at the surface. The system of dikes, rather than a single large equidimensional storage chamber, favors efficient degassing due to the relatively small width dimensions of the dikes [*Eichelberger et al.*, 1986] and a significant portion of the degassed materials accumulate in a shallow poroelastic storage chamber (C_3). Excess pore pressure in C_3 decays following a degassing event.

[42] Of course, in the absence of other data, the transient source strength behavior could be interpreted with alternative models. First, because the eruption itself requires magma transport, the sources could be due entirely to magma injection into three separate chambers. We reject this model because it requires unlikely magma transport and storage back and forth among the three chambers during the posteruption phase. Second, the posteruption behavior of C_2 could also be poroelastic, although this is not consistent with the accelerating magma influx into C_1 because the source strength of C_2 should also experience a reversal from

contraction to expansion. The posteruption behavior of C_3 could be due to thermoelastic contraction and expansion during early and late posteruption phases. However, C_3 is very shallow and therefore we expect pore fluid flow would act as a heat sink and modulate thermoelastic effects. Model B is our favored model because it is consistent with deformation data, petrologic evidence, and mechanics of the regional-scale tectonic system.

7. Conclusions

[43] The source cluster method, combined with multiple InSAR images, allows us to infer the quantitative spatial and temporal behavior of volcano deformation sources. Additionally, the method requires neither specialized a priori source geometric configurations (e.g., point, tabular, or ellipsoidal sources) nor a particular presuposed linear deformational mechanism (e.g., magma intrusion, poroelasticity, or thermoelasticity).

[44] Generating regularized incremental time series does not require an a priori time-dependent function [*Lu et al.*, 2003a] and serves to reduce artifacts due to atmospheric anomalies in the InSAR data. Although we could fit the transient behavior of clusters to high order polynomial functions, the method used does not require an explanation of the physical significance of such functions.

[45] Several plausible interpretations of the cluster behavior are possible based on the InSAR data alone. Although independently derived from deformation data, the spatial and temporal behavior of the clusters interpreted using model B is compatible with the magmatic system model proposed by *Singer et al.* [1992b]. This model reduces an apparently complex cacophony of unrelated events into a simple system of interrelated predictable processes driven by magma dynamics.

[46] **Acknowledgments.** ERS-1/ERS-2 SAR images are copyright 1992–2000 ESA and provided by the Alaska SAR Facility (ASF). This research was supported by funding from NASA (NRA-99-OES-10 RADARSAT-0025-0056) and in part by the USGS contracts O3CRCN0001 and 1434-CR-97-CN-40274. The SRTM data were processed by NASA JPL for NIMA and provided by the USGS EROS Data Center. We thank the User Service of ASF for their special efforts to provide SAR data on a timely basis, and D-PAF/ESA for providing precise satellite orbit information. We thank J. Power for discussions of the 1992–1993 eruption of Seguam, T. Wright for help on developing the quadtree algorithm, and C. Wicks on discussion of inversion methods. S. Moran and M. Poland provided technical reviews. Constructive comments from the Associate Editor Freysteinn Sigmundsson and an insightful review by Geoff Wadge greatly improved this paper.

References

Beauducel, F., P. Briole, and J. L. Froger (2000), Volcano-wide fringes in ERS satellite radar interferograms of Etna (1992–1998): Deformation or tropospheric effect?, *J. Geophys. Res.*, *105*, 16,391–16,402.

Dzurisin, D. (2003), A comprehensive approach to monitoring volcano deformation as a window on the eruption cycle, *Rev. Geophys.*, *41*(1), 1001, doi:10.1029/2001RG000107.

Eichelberger, J. C., C. R. Carrigan, H. R. Westrich, and R. H. Price (1986), Non-explosive silicic volcanism, *Nature*, *323*, 598–602.

Farr, T. G., and M. Kobrick (2000), Shuttle radar topography mission produces a wealth of data, *Eos Trans. AGU*, *81*(48), 583, 585.

Feigl, K. L., J. Gasperi, F. Sigmundsson, and A. Rigo (2000), Crustal deformation near Hengill volcano, Iceland 1993–1998: Coupling between magmatic activity and faulting inferred from elastic modeling of satellite radar interferograms, *J. Geophys. Res.*, *105*, 25,655–25,670.

Fialko, Y., and M. Simons (2000), Deformation and seismicity in the Coso geothermal area, Inyo County, California: Observations and modeling using satellite radar interferometry, *J. Geophys. Res.*, *105*, 21,781–21,794.

Freymueller, J., N. E. King, and P. Segall (1994), The co-seismic slip distribution of the Landers earthquake, *Bull. Seismol. Soc. Am.*, *84*, 646–659.

Geist, E. L., J. R. Childs, and D. W. Scholl (1988), The origin of summit basins of the Aleutian Ridge: Implications for block rotation of an arc massif, *Tectonics*, *7*, 327–341.

Grow, J. A. (1973), Crustal and upper mantle structure of the central Aleutian arc, *Geol. Soc. Am. Bull.*, *84*, 2169–2192.

Lu, Z., and M. Wyss (1996), Segmentation of the Aleutian plate boundary derived from stress direction estimates based on fault plane solutions, *J. Geophys. Res.*, *101*, 803–816.

Lu, Z., D. Mann, J. T. Freymueller, and D. J. Meyer (2000a), Synthetic aperture radar interferometry of Okmok volcano, Alaska: Radar observations, *J. Geophys. Res.*, *105*, 10,791–10,806.

Lu, Z., J. A. Power, and D. Dzurisin (2000b), Ground deformation associated with the March 1996 earthquake swarm at Akutan volcano, Alaska, revealed by satellite radar interferometry, *J. Geophys. Res.*, *105*, 21,483–21,495.

Lu, Z., T. Masterlark, J. Power, D. Dzurisin, C. Wicks, and W. Thatcher (2002), Subsidence at Kiska volcano, western Aleutians, detected by satellite radar interferometry, *Geophys. Res. Lett.*, *29*(3), 1855, doi:10.1029/2002GL014948.

Lu, Z., T. Masterlark, D. Dzurisin, R. Rykhus, and C. Wicks Jr. (2003a), Magma supply dynamics at Westdahl volcano, Alaska, modeled from satellite radar interferometry, *J. Geophys. Res.*, *108*(B7), 2354, doi:10.1029/2002JB002311.

Lu, Z., C. Wicks, D. Dzurisin, J. Power, W. Thatcher, and T. Masterlark (2003b), Interferometric synthetic aperture radar studies of Alaska volcanoes, *Earth Obs. Mag.*, *12*, 8–18.

Lundgren, P., and P. A. Rosen (2003), Source model for the 2001 flank eruption of Mt. Etna volcano, *Geophys. Res. Lett.*, *30*(7), 1388, doi:10.1029/2002GL016774.

Mann, D., and J. Freymueller (2003), Volcanic and tectonic deformation on Unimak Island in the Aleutian Arc, Alaska, *J. Geophys. Res.*, *108*(B2), 2108, doi:10.1029/2002JB001925.

Massonnet, D., and K. Feigl (1998), Radar interferometry and its application to changes in the Earth's surface, *Rev. Geophys.*, *36*, 441–500.

Masterlark, T. (2003), Finite element model predictions of static deformation from dislocation sources in a subduction zone: Sensitivities to homogeneous, isotropic, Poisson-solid, and half-space assumptions, *J. Geophys. Res.*, *108*(B11), 2540, doi:10.1029/2002JB002296.

Menke, W. (1989), *Geophysical Data Analysis: Discrete Inverse Theory*, *Int. Geophys. Ser.*, vol. 45, 289 pp., Academic, San Diego, Calif.

Miller, T. P., R. G. McGimsey, D. H. Richter, J. R. Riehle, C. J. Nye, M. E. Yount, and J. A. Dumoulin (1998), Catalog of the historically active volcanoes of Alaska, *U.S. Geol. Surv. Open File Rep., 98–582*, 104 pp.

Mogi, K. (1958), Relations between the eruptions of various volcanoes and the deformations of the ground surface around them, *Bull. Earthquake Res. Inst. Univ. Tokyo*, *36*, 99–134.

Mossop, A., and P. Segall (1999), Volume strain within the Geysers geothermal field, *J. Geophys. Res.*, *104*, 29,113–29,131.

Nowacki, W. (1986), *Thermoelasticity*, 566 pp., Pergamon, New York.

Press, W., S. Teukolsky, W. Vetterling, and B. Flannery (1992), *Numerical Recipes in C, the Art of Scientific Computing*, 994 pp., Cambridge Univ. Press, New York.

Rosen, P. A., et al. (2000), Synthetic aperture radar interferometry, *Proc. IEEE*, *88*, 333–380.

Ryan, H. F., and D. W. Scholl (1993), Geological implications of great interplate earthquakes along the Aleutian arc, *J. Geophys. Res.*, *98*, 22,135–22,146.

Samet, H., and R. E. Webber (1988), Hierarchical data structures and algorithms for computer graphics. I. Fundamentals, *IEEE Comput. Graphics Appl.*, *8*(3), 48–68.

Singer, B. S., and T. H. Pearce (1993), Plagioclase zonation in a basalt to rhyodacite eruptive suite, Seguam Island, Alaska: Observations by Nomarski contrast interference, *Can. Mineral.*, *31*, 459–466.

Singer, B. S., J. D. Meyers, and C. D. Frost (1992a), Mid-Pleistocene basalt from the Seguam volcanic center, central Aleutian arc, Alaska: Local lithospheric structures and source variability in the Aleutian arc, *J. Geophys. Res.*, *97*, 4561–4578.

Singer, B. S., J. D. Meyers, and C. D. Frost (1992b), Mid-Pleistocene lavas from Seguam volcanic center, central Aleutian arc: Closed-system fractional crystallization of a basalt to rhyodacite eruptive suite, *Contrib. Mineral. Petrol.*, *110*, 87–112.

Singer, B. S., T. H. Pearce, A. M. Kolisnik, and J. D. Meyers (1993), Plagioclase zoning in mid-Pleistocene lavas from the Seguam volcanic center, central Aleutian arc, Alaska, *Am. Mineral.*, *78*, 143–157.

Spera, F. J. (2000), Physical properties of magma, in *Encyclopedia of Volcanoes*, edited by H. Sigurdsson, pp. 171–190, Academic, San Diego, Calif.

Turcotte, D. L., and G. J. Schubert (1982), *Geodynamics: Applications of Continuum Physics to Geological Problems*, 450 pp., John Wiley, Hoboken, N. J.

Vasco, D. W., C. Wicks Jr., K. Karasaki, and O. Marques (2002), Geodetic imaging: Reservoir monitoring using satellite interferometry, *Geophys. J. Int.*, *149*, 1–16.

Wang, H. F. (2000), *Theory of Linear Poroelasticity With Applications to Geomechanics*, 287 pp., Princeton Univ. Press, Princeton, N. J.

Wang, H. F., and M. P. Anderson (1982), *Introduction to Groundwater Modeling: Finite Difference and Finite Element Methods*, 237 pp., Academic, San Diego, Calif.

Wicks, C. W., W. Thatcher, F. C. Monastero, and M. A. Hasting (2001), Steady state deformation of the Coso Range, east central California, inferred from satellite radar interferometry, *J. Geophys. Res.*, *106*, 13,769–13,780.

Wicks, C. W., D. Dzurisin, S. Ingebritsen, W. Thatcher, Z. Lu, and J. Iverson (2002), Magmatic activity beneath the quiescent Three Sisters volcanic center, central Oregon Cascade Range, USA, *Geophys. Res. Lett.*, *29*(7), 1122, doi:10.1029/2001GL014205.

Williams, C. A., and G. Wadge (1998), The effects of topography on magma chamber deformation models: Application to Mt. Etna and radar interferometry, *Geophys. Res. Lett.*, *25*, 1549–1552.

Zebker, H. A., P. A. Rosen, R. M. Goldstein, A. Gabriel, and C. L. Werner (1994), On the derivation of coseismic displacement fields using differential radar interferometry: The Landers earthquake, *J. Geophys. Res.*, *99*, 19,617–19,634.

Z. Lu and T. Masterlark, U.S. Geological Survey EROS Data Center, 47914 252nd St., Sioux Falls, SD 57198, USA. (lu@usgs.gov; masterlark@usgs.gov)